

Zero- to Low-field Relaxometry of Chemical and Biological Fluids

Seyma Alcicek^{*1,2,+}, Piotr Put^{1,+}, Adam Kubrak³, Fatih Celal Alcicek⁴, Danila Barskiy^{5,6}, Stefan Gloeggler⁷, Jakub Dybas⁴, and Szymon Pustelny^{*1}

¹Institute of Physics Faculty of Physics, Astronomy and Applied Computer Science, Jagiellonian University in Kraków, 11 Stanisława Lojasiewicza St., 30-348, Kraków, Poland

²Institute of Neuroradiology, University Hospital Frankfurt, Goethe University, Frankfurt, 60528, Germany

³Faculty of Chemistry, Jagiellonian University in Kraków, 2 Gronostajowa St., 30-387, Krakow, Poland

⁴Jagiellonian Center for Experimental Therapeutics, Jagiellonian University in Kraków, 14 Bobrzynskiego St., 30-348, Kraków, Poland

⁵Helmholtz Institute Mainz, GSI Helmholtz Center for Heavy Ion Research GmbH, 55128 Mainz, Germany

⁶Institute of Physics, Johannes Gutenberg-Universität, 55128 Mainz, Germany

⁷Max Planck Institute for Multidisciplinary Sciences, Am Fassberg 11, 37077, Göttingen, Germany

*seyma.alcicek@kgu.de

*szymon.pustelny@uj.edu.pl

+these authors contributed equally to this work

ABSTRACT

NMR relaxometry is an analytical method that provides information about the molecular environment, including even NMR “silent” molecules (spin-0), by analyzing the properties of NMR signals versus the magnitude of the longitudinal field. Conventionally, this technique has been performed at fields much higher than Earth’s magnetic field, but in this work, we present NMR relaxometry at zero and ultra-low magnetic fields (ZULFs). Operation under ZULFs allows us to investigate many slow (bio)chemical processes, whose timescale (milliseconds-seconds) coincides with a timescale of spin evolution. ZULFs regime also limits the detrimental role of T_2 dephasing, which, in heterogeneous samples, is induced by magnetic susceptibility and often leads to line broadening, hence low-resolution spectra. Finally, in contrast to their high-field NMR, ZULF NMR measurements can be performed with inexpensive, portable/small-size sensors (atomic magnetometers). Here, we use ZULF NMR relaxometry in the analysis of (bio)chemical compounds containing ^1H - ^{13}C , ^1H - ^{15}N , and ^1H - ^{31}P spin pairs. We also detected high-quality ULF NMR spectra of human whole blood at $0.8\ \mu\text{T}$, despite a shortening of spin relaxation by blood proteomes (e.g., hemoglobin). Information on relaxation times of blood, a potential early biomarker of inflammation, can be obtained in less than a minute and without the need for a sophisticated apparatus.

Introduction

Nuclear magnetic resonance (NMR) relaxometry is a method that allows one to characterize the physical and dynamic properties of samples by analyzing nuclear-spin relaxation^{1,2}. Measurements of the longitudinal relaxation time T_1 , governing the restoration of thermal equilibrium in a sample (corresponding to the growth of static magnetization in high-field NMR), and the transverse relaxation time T_2 (determining the decay of oscillating transverse magnetization) provide valuable information about sample environment. In contrast to NMR spectroscopy, relaxometry can be performed with cheaper lower-field magnets as generally there is no need to obtain a well-resolved NMR spectrum³. This approach has been used in agricultural⁴, petrochemical⁵, and food⁶ sciences, as well as in the analysis of biological samples⁷.

In addition to conventional (high-field) NMR relaxometry studies, NMR relaxometry at (ultra-)low magnetic fields (ULFs) has been recently demonstrated⁸⁻¹⁰. This became possible due to the application of non-inductive sensors, which are sensitive to low-frequency magnetic signals (particularly in the sub-kilohertz range)^{11,12}. Specifically, atomic magnetometers—offering high near-DC sensitivity, low price, small size, and non-cryogenic operation—have recently been used for such measurements^{13,14}. In ULFs, proton Larmor frequencies are in the range where they overlap with the rate of many slow biochemical processes of interest that occur on the microsecond to millisecond time scale^{15,16} such as protein folding^{17,18}, ligand binding¹⁹, membrane transport²⁰, intramolecular diffusion²¹, oxidation-reduction reactions^{22,23}, and chemical exchange in biomolecules²⁴. Therefore, compared to conventional NMR relaxometry, operation at ULFs enables the study of slow processes, as the spin evolution in this field regime occurs at similar timescales. Furthermore, the study of NMR samples in this field regime is

especially interesting, as the relaxation properties strongly depend on the magnetic-field strength. This allows for the direct determination of molecular motion parameters¹⁴.

NMR relaxometry can provide information on paramagnetic as well as diamagnetic (e.g., proteins) compounds in solution^{10,25}. Blood is one of the attractive biological specimens for relaxometry studies. By probing the T_2 relaxation of water protons, NMR relaxometry of blood samples has been shown to hold great promise in the diagnosis and prognosis of metabolic disorders (insulin resistance, dyslipidemia), infections (candidiasis, malaria) and hemostatic disorders^{3,26,27}. Furthermore, relaxation of water protons in blood can provide valuable information about blood proteomes as water protons form hydrogen bonds with proteins, lipoproteins, and metabolites, affecting spin relaxation. While the contribution of macromolecules (e.g., proteins and lipoproteins) to proton relaxation is considerable, the influence of small metabolites (e.g., glucose and amino acids) on the process can be neglected due to the fast molecular motion, leading to inefficient dipolar relaxation^{3,28}. This may allow us to observe inflammatory-induced protein profile variations, independent of minor metabolites whose concentration may vary in an unrelated manner. Although variation in the molecular weight profile of blood proteins also affects the relaxation rate, in general, a linear correlation between protein concentration and relaxation rate is expected due to slower rotational and diffusion mobility of macromolecules²⁹. Consequently, the existence of a strong correlation between proton relaxation times and protein content makes T_1 and T_2 values promising biomarkers³⁰.

In this paper, the investigation of NMR relaxometry of chemical and biological samples in zero and (ultra-)low magnetic fields (ZULFs) is presented. First, the effect of dissolved paramagnetic oxygen on relaxation times is examined in strongly coupled heteronuclear systems at zero field. This is achieved by the analysis of zero-field NMR J -spectra³¹, where peaks' positions are determined by the ^1H - ^{31}P and ^1H - ^{13}C J -couplings. Second, the influence of solvents (H_2O and D_2O) on relaxation process is studied in ULFs by monitoring the longitudinal relaxation of protons coupled to long-lived ^{15}N in methylpyridinium. Third, NMR spectra of water solutions with different concentrations (0.2-1 mM) of CuSO_4 , which are particularly interesting for quantitative imaging studies using phantoms (to mimic biological samples)³², are used to study the influence of paramagnetic agents on water-proton relaxation under ULFs (10-510 μT). Finally, nuclear magnetic relaxation dispersion (NMRD) profiles of protons in human whole blood and plasma are investigated at ULFs to demonstrate the potential of the ZULF NMR relaxometry method for the analysis of biological samples.

Results and Discussion

Effect of Oxygen on Zero-field NMR

Oxygen molecules, being paramagnetic (i.e., containing unpaired electrons), influence nuclear spin relaxation³³. Therefore, to avoid oxygen-induced relaxation, liquid NMR samples are often degassed. This is achieved by purging the samples with neutral gas (e.g., nitrogen) or by the freeze-pump-thaw technique and subsequent flame sealing. Despite the fact that this procedure is routinely used, its significance on ZULF NMR spectra has never been investigated. To fill this gap, we studied this effect by analyzing the amplitudes and widths of peaks observed in zero-field NMR J -spectra^{14,34}, which provide information about the longitudinal (T_1) and transverse (T_2) relaxation times.

First, we examined trimethyl phosphate solutions prepared with a procedure that involves a different number of freeze-pump-thaw cycles. As trimethyl phosphate consists of nine equivalent protons coupled to phosphorus (with coupling constant $J_{\text{HP}}=11$ Hz), its zero-field spectrum consists of peaks at J_{HP} , $2J_{\text{HP}}$, $3J_{\text{HP}}$, $4J_{\text{HP}}$, and $5J_{\text{HP}}$ (see detailed discussion of trimethyl phosphate spectrum at zero field in Ref.³⁴). Here, due to the relatively low amplitude of the peaks at 11 and 55 Hz, we only analyzed the peaks at 22, 33, and 44 Hz. As demonstrated in Fig. 1a, a substantial increase in the amplitude of the peaks and a decrease in their linewidth were observed up to two freeze-pump-thaw cycles. Although cycling initially helps to reduce the peak linewidth, the results also show that no significant differences in the signal parameters were observed by increasing the number of cycles above two (Fig. 1b). Changes in peak linewidths and therefore molecule relaxation time T_2 are associated with the reduction of paramagnetic oxygen in the sample. Most likely, after two cycles, an oxygen level in the solution is small (potentially negligible) in terms of its contribution to relaxation. Therefore, no improvement in the signal was achieved after the second cycle. Alternatively, even though the vacuum pump can reduce pressure over the frozen liquid to about 10^{-6} mbar, it might be insufficient to remove remaining dissolved oxygen any further after two cycles.

As the next step, we investigated the influence of paramagnetic oxygen on heteronuclear long-lived spin singlet states, which are protected from intramolecular dipolar relaxation between the two spins³⁵. In high-field NMR, this state has been demonstrated for homonuclear spin-1/2 pairs (e.g., parahydrogen), where two coupled spins are magnetically equivalent, and hence can constitute a spin-0 (singlet) and a spin-1 (triplet) systems. The triplet states are symmetric, and the singlet state is anti-symmetric with respect to particle interchange. Since the main relaxation mechanism, originating from the dipolar

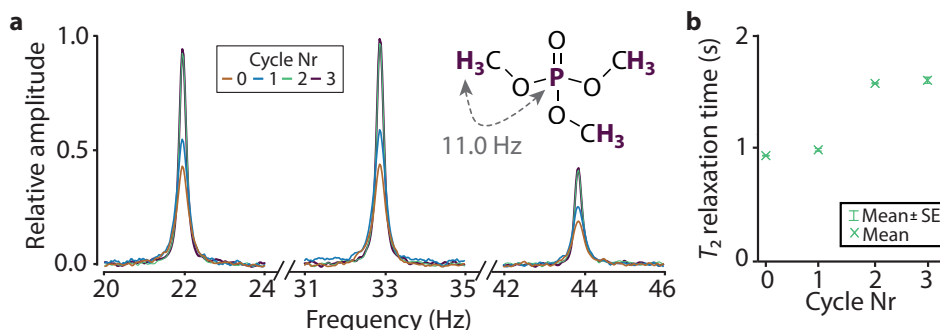


Figure 1. (a) Zero-field NMR J -spectra (showing resonances at $2J_{\text{HP}}$, $3J_{\text{HP}}$ and $4J_{\text{HP}}$) of the trimethyl phosphate samples prepared with a different number of freeze-pump-thaw cycles (0, 1, 2, and 3). (b) Extracted transverse relaxation time T_2 of trimethyl phosphate in zero magnetic field versus the number of freeze-pump-thaw cycles performed during the sample preparation. Each experimental point is a mean relaxation rate extracted from three peaks shown in (a).

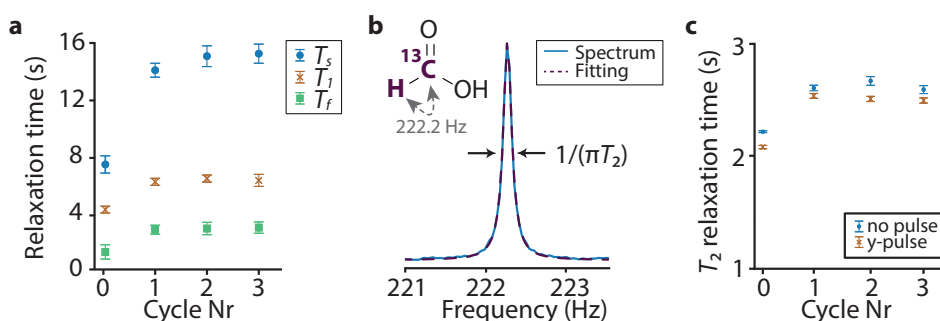


Figure 2. (a) Relaxation times T_1 , T_f , and T_s (see the text for explanation) of ^{13}C -formic acid as a function of the number of freeze-pump-thaw cycles performed during the sample preparation. (b) Lorentzian fit (dashed line) of the zero-field NMR signal of ^{13}C -formic acid (solid blue line) at 222.2 Hz. (c) Comparison between the transverse relaxation times measured after a non-adiabatic transfer to zero field with (orange crosses) and without (blue circles) a complimentary y -pulse.

coupling, is invariant upon exchange of two spins, it is unlikely to cause a singlet-triplet breaking-symmetry transition; thus, the dipole-dipole coupling cannot contribute to relaxation of the singlet state³⁵. At a zero magnetic field, coupled heteronuclear spin-1/2 pairs can form singlet states as well³⁶. Specifically, zero-field heteronuclear singlet states have been previously reported in ^{13}C -formic acid and $^{13}\text{C}_1$ -benzene with tens of seconds of lifetimes³⁶, which are significantly longer than the longitudinal relaxation times T_1 .

^{13}C -formic acid is one of the standard samples for ZULF NMR due to its long relaxation time and simple molecular structure. The zero-field spectrum of ^{13}C -formic acid consists of a single peak at about 222.2 Hz, which is the strength of the one-bond ^1H - ^{13}C coupling, while the hydroxyl-group proton coupling is negligible due to a fast proton exchange. As discussed in detail in Ref.³⁶, after thermal prepolarization with the permanent magnet, the sample is transferred to the ULF region, where it is stored in the guiding (storage) field for a given time. Next, the field is suddenly switched off ($\approx 10 \mu\text{s}$) to provide a non-adiabatic transfer to the zero field where singlet-triplet spin system occurs and hence generate coherences between the $|T_0\rangle$ (total quantum number $F = 1$, magnetic quantum number $M_F = 0$) and $|S_0\rangle$ ($F = 0$, $M_F = 0$) states (see Ref³⁷ for a detailed explanation). As described above, the measurements of the width of the ZULF NMR resonances provide access to the transverse relaxation time T_2 , while the dependence of peak amplitudes on the storage time gives information about the longitudinal relaxation time T_1 . In the considered case, the longitudinal relaxation is determined by the so-called slow and fast relaxation, characterized by the relaxation times T_s and T_f , respectively³⁶. The fast decay is caused by the equalization of the population between three triplet magnetic sublevels ($|T_{-1}\rangle$ ($F = 1$, $M_F = -1$), $|T_0\rangle$, and $|T_{+1}\rangle$ ($F = 1$, $M_F = +1$)), and the slow relaxation is associated with thermalization among the singlet and triplet states. Thereby, the bi-exponential fit to the amplitude data provides information about both relaxation times. Alternatively, relaxation may be investigated by sudden switching off of the leading field and successive application of the pulse of a magnetic field oriented along the y -axis while the magnetometer is sensitive along the z -axis (see details in the Methods section). In this case, the amplitude of the signal is proportional to the population difference between the $|T_{+1}\rangle$ and $|T_{-1}\rangle$ states³⁸. In turn, signal decay is only determined by the

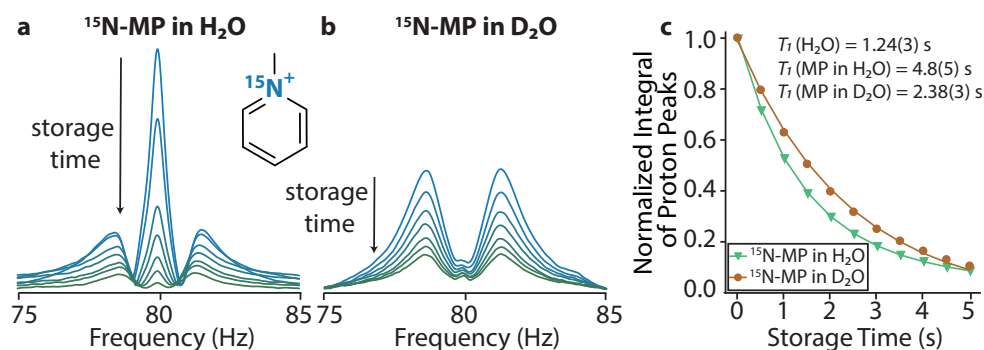


Figure 3. ULF NMR spectra of ^{15}N -methylpyridinium (^{15}N -MP) in (a) H_2O and (b) D_2O measured after different storage times. The peak at ≈ 80 Hz corresponds to the Larmor precession frequency of water protons while the satellite peaks correspond to the Larmor precession of ^{15}N -MP protons (coupled to ^{15}N). (c) Decay of the proton signals shown in (a), ^{15}N -MP plus H_2O peaks (green triangles) and the proton signals shown in (b), the ^{15}N -MP peaks in D_2O (red circles), as a function of storage time. The solid lines are the fit overlaying the data points. For the case of ^{15}N -MP dissolved in D_2O , the line is a monoexponential decay with T_1 time of 2.38(3) s. For the case of ^{15}N -MP dissolved in H_2O , the line is a bi-exponential decay with T_1 times of 4.8(5) s and 1.24(3), for ^{15}N -MP and water protons, respectively.

lifetime of the triplet states, and hence the relaxation time T_1 can be determined from a single exponent fitting to the amplitude decay (see Methods).

To study the influence of the amount of dissolved paramagnetic oxygen on the relaxation process mentioned above, we measured the zero-field NMR spectra of ^{13}C -formic acid solutions following different numbers of freeze-pump-thaw cycles (Fig. 2a). The T_2 values extracted (as demonstrated with the example spectrum in Fig. 2b) for the schemes described above (i.e., with non-adiabatic switching off the field and with the transverse y -pulse) are shown in Fig. 2c. An increase in all relaxation times (to a greater extent in the case of T_2) is observed when a single and two freeze-pump-thaw cycles are performed. This is due to the efficient removal of oxygen from the samples. However, there is no significant effect of the third cycle on relaxation terms as in the case of trimethyl phosphate. It should be noted that the longest relaxation time we measured is shorter than the ones reported in Ref.³⁶. The reason is that even though there is no signal associated with the proton of the hydroxyl group, the contribution of this exchangeable proton to the polarization relaxation is non-negligible³⁹. In fact, increasing the proton-exchange rate enables elimination of this relaxation mechanism. However, in our study, we used neat ^{13}C -formic acid (95% in weight in H_2O), in contrast to the previous study where water and acetonitrile were mixed to accelerate the chemical exchange process. A further increase in the exchange rate leads to the decoupling of the hydroxyl-group proton from the $^{13}\text{CH}_3$ group, prolonging the relaxation time and affecting the zero-field spectra, as demonstrated in Refs.^{39,40}. It should be also noted that the experiments with a non-adiabatic transfer result in narrower zero-field peaks compared to the measurements with an additional transverse pulse, which is an indicator of a longer T_2 value. This finding could be explained by the generation of coherences between the $|T_0\rangle$ and long-lived $|S_0\rangle$ states after non-adiabatic transfer, as mentioned above. On the other hand, the application of transverse pulse increases the intensity of the signal³⁴.

To summarize, it is demonstrated that the presence of paramagnetic oxygen molecules has a crucial impact on ZULF NMR spectra and it should be taken into account in quantitative ULF relaxometry experiments. This finding also suggests the potential use of ZULF NMR relaxometry in the evaluation of paramagnetic gas impurities^{41,42}.

Solvent effect in ULF NMR Relaxometry

Relaxation measurements can also be performed under low-field conditions, i.e., in the regime where the Zeeman interaction begins to dominate over the scalar couplings^{43,44}. This is illustrated in the ultra-low field spectra of ^{15}N -methylpyridinium (^{15}N -MP) obtained under a magnetic field of 1.88 μT which is precursor of pyridinium-derived compounds. Due to the long (several minutes) lifetime of ^{15}N nuclei, biocompatibility, and the ability to be hyperpolarized in water, these compounds have been proposed as magnetic-resonance-imaging contrast agents⁴⁵. We investigated ^{15}N -MP in both H_2O and D_2O solutions, which allowed us to study the role of a solvent on longitudinal relaxation at ULF conditions.

Figure 3a shows the spectrum of ^{15}N -MP dissolved in H_2O . The spectrum consists of a strong peak at about 80 Hz, arising from water protons, and two broader satellite humps, symmetric around the proton peak (75-85 Hz). The latter are groups of

overlapping peaks, originating from the precession of ^{15}N -MP protons coupled to ^{15}N . When the storage time (in a storage field of $10\ \mu\text{T}$) was increased, a water-proton peak decayed faster than the ^{15}N -MP peaks (Fig. 3a). This reveals a shorter longitudinal relaxation time of the water protons than for the ^{15}N -MP protons. To calculate the T_1 lifetimes of the protons, data points, corresponding to the normalized integration values of proton peaks in the 75–85 Hz frequency range, were plotted as a function of the storage time (Fig. 3c). Due to the overlap between the water- and MP-proton peaks, the data (denoted by green triangles) was fit to bi-exponential decay. This allowed us to determine the ^{15}N -MP and water-proton relaxation times as 4.8(5) and 1.24(3) s, respectively. A similar study was performed for ^{15}N -MP dissolved in D_2O , where only the ^{15}N -MP peaks were observed. Figure 3c shows the amplitude of the peak measured at 81 Hz versus the storage time. This data was fit with a single exponential decay and the longitudinal relaxation time T_1 of 2.38(3) s was determined. These results reveal an interesting effect of the shorter relaxation time of ^{15}N -MP protons in water compared to that in the deuterated solution. A similar solvent effect on the T_1 relaxation of both ^{15}N and ^1H in ^{15}N -MP was also observed in high-field NMR (see Supplementary Information). This result might be explained by the isotope effect in which the solvents differ in their hydrogen bonding characteristics and the formation of the solvation spheres^{46,47}. In addition, lower mobility of D in D_2O compared to H in H_2O may result in slower dipole reorientation, hence a higher relaxation rate is expected in D_2O , especially of small ionic compounds⁴⁸. Despite these speculations, better understanding of relaxation mechanisms of coupled spin systems at ZULF conditions needs further studies.

One should point out that low-frequency peaks of ^{15}N nuclei that are coupled to the protons were not visible in the ULF spectra of ^{15}N -MP. This is not surprising because, due to low gyromagnetic ratio of ^{15}N nuclei, the signal from coupled ^{15}N -spin precession in the ULF regime is expected to be approximately two orders of magnitude smaller than the signals from protons. To remedy that, parahydrogen-based hyperpolarization techniques can be employed to study ^{15}N nuclei under the ZULF regime even using unlabeled compounds (natural abundance of $^{15}\text{N} = 0.36\%$) as it was recently demonstrated^{49,50}.

Paramagnetic Relaxation in ULF NMR

To demonstrate the feasibility of ULF NMR relaxometry for the analysis of biological samples, aqueous solution of paramagnetic copper sulfate, CuSO_4 , widely used for quantitative imaging studies, was investigated. This compound was used to prepare phantoms that mimic biological samples with short relaxation times³². Water-proton precession was observed to gather information about the T_1 and T_2 proton relaxation, which is accelerated by the presence of paramagnetic ions in the solution. During the ULF spectra acquisition, the NMR sample was subjected to a detection field of $0.8\ \mu\text{T}$, corresponding to proton Larmor frequency of about 34 Hz. In Fig. 4a, ULF NMR spectra corresponding to water-proton precession, are shown for different storage times in a field of $10\ \mu\text{T}$. The effect of CuSO_4 is observed as a broadening of the ULF NMR peak (Fig. 4a). The longitudinal ($1/T_1$) and transverse ($1/T_2$) relaxation rates, measured for water in different CuSO_4 concentrations, are shown in Fig. 4b–d. The data demonstrate that the presence of up to 1 mM of paramagnetic CuSO_4 accelerated the longitudinal and transverse relaxation by an order of magnitude. According to the general relaxation theory⁵¹, the $1/T_1$ and $1/T_2$ relaxation rates are proportional to the concentration of the paramagnetic species and can be calculated by adding the paramagnetic and diamagnetic relaxation rates. Following this approach, T_2 relaxivity of CuSO_4 is calculated as $1.04(5)\ \text{s}^{-1}/\text{mM}$ (Fig. 4b). T_1 relaxivity of CuSO_4 is studied for magnetic fields between $10\ \mu\text{T}$ and $510\ \mu\text{T}$, which allowed us to reconstruct the NMRD profiles (Fig. 4c,d).

The longitudinal relaxation rates $1/T_1$, derived from ULF NMR measurements with non-degassed CuSO_4 water solutions (flame-sealed without the freeze-pump-thaw procedure), are presented in Fig. 4c. Overall, no significant dependence of the longitudinal relaxation rate on the magnetic-field strength was observed. The extracted T_1 relaxivity of CuSO_4 was $1.0(1)\ \text{s}^{-1}/\text{mM}$. On the other hand, measurements with the non-degassed pure water solution (bottom dashed line in Fig. 4c) and degassed CuSO_4 water solutions (Fig. 4d) show that the gradual increase of the storage field from $10\ \mu\text{T}$ to $510\ \mu\text{T}$ resulted in a continuous decrease in the longitudinal relaxation rate $1/T_1$. The possible explanation for this difference can be the simultaneous presence of paramagnetic oxygen and CuSO_4 in solutions. This may accelerate the relaxation process resulting in the disappearance of the weak dependence of water-proton relaxation on the storage field in the ULF regime. T_1 relaxivity of CuSO_4 is calculated as $1.10(5)\ \text{s}^{-1}/\text{mM}$ using $1/T_1$ values averaged over different magnetic fields. In both cases, T_1 relaxivity constant of CuSO_4 in water are in good agreement with literature values obtained in high magnetic field⁵².

To test the detection limit of ULF NMR relaxometry, even higher concentrations of CuSO_4 were studied. In water samples containing 1.5 and 2 mM of CuSO_4 , stored in a field of $10\ \mu\text{T}$, the longitudinal relaxation times T_1 of protons were 0.38(5) and 0.363(7) s, respectively. It should be stressed that, despite the fast relaxation, the water-proton peak was clearly visible in the ULF NMR spectrum, allowing relaxation studies. Since the proton relaxation time of the blood is short as well, i.e., on the order of hundreds of milliseconds (see below), this phantom study has shown the feasibility of ULF NMR relaxometry of blood using an atomic magnetometer³.

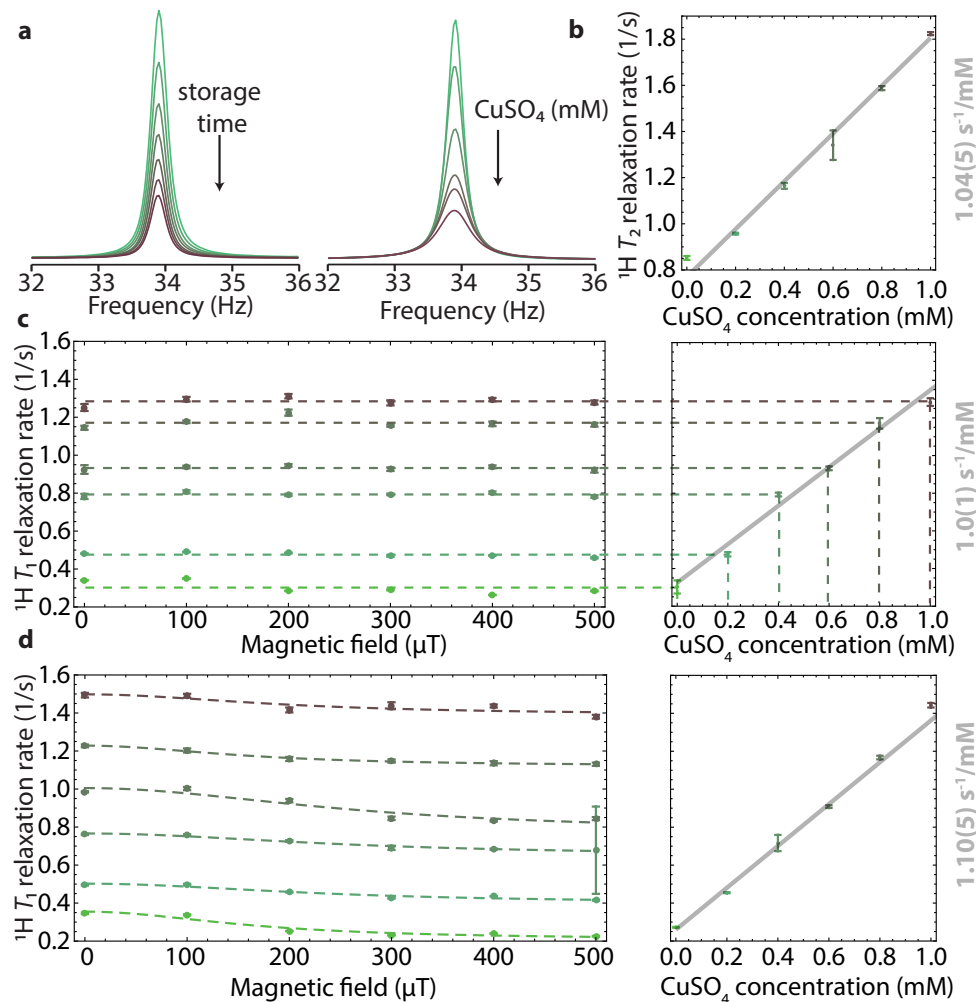


Figure 4. (a) ULF NMR proton spectra of aqueous solutions of CuSO_4 measured in a field of $0.8 \mu\text{T}$. The water-proton peak is shown as a function of the storage time (without CuSO_4 added) and as a function of CuSO_4 concentration; the storage field was $10 \mu\text{T}$. (b) T_2 relaxation rate as a function of the CuSO_4 concentration (obtained from the average of vacuumed and non-vacuumed samples) and the linear fit with the extracted value of relaxivity. (c) Longitudinal relaxation rate $1/T_1$ of the water proton in CuSO_4 solutions without and (d) with degassing prior to the measurements as a function of the magnetic field (left panel) and CuSO_4 concentration (right panel). The dashed line in the field profile corresponds to the fit of Lorentzian function $T_1^{-1}(B) = T_1^{-1}(0)/(1 + (\gamma B)^2 \tau_c^2)$ ¹⁴, with the correlation time τ_c set to $18 \mu\text{s}$, providing an adequate match to observed experimental results. The relaxivity values are extracted from the linear fit to the average relaxation rates for various concentrations of CuSO_4 across different magnetic fields.

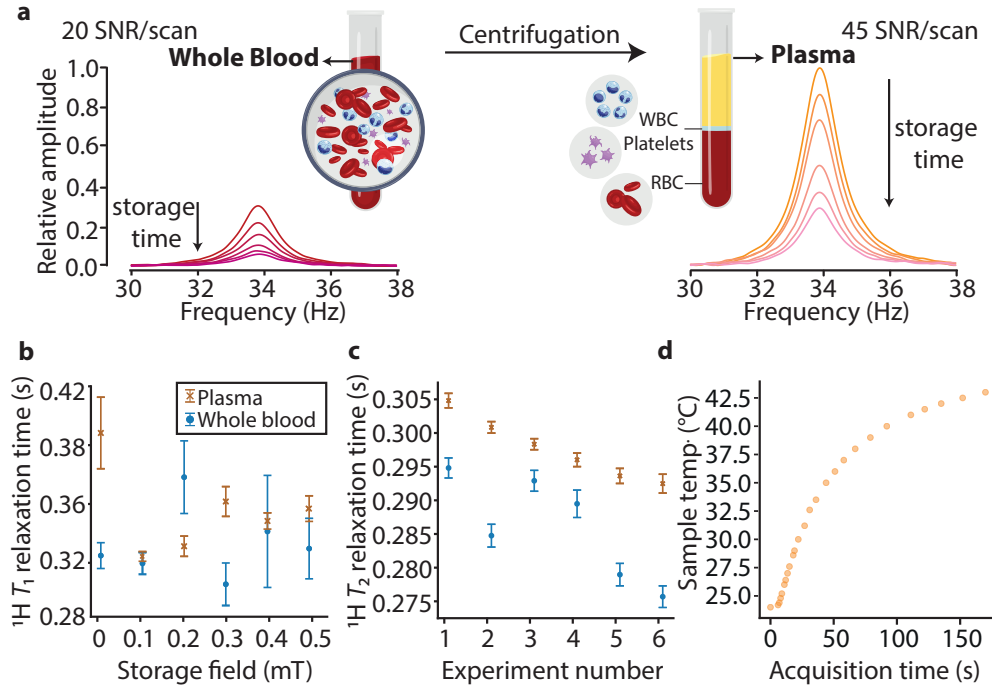


Figure 5. (a) Proton ULF NMR signals from human whole-blood (left) and blood-plasma (right) samples shown as a function of storage time at the 10 μT field. Transverse magnetic field during the detection was 0.8 μT . Signal-to-noise ratio (SNR) per scan is indicated for each sample. (b) T_1 and (c) T_2 relaxation times of human whole blood and blood plasma at ULFs (taken at the storage fields between 10 and 510 μT). It was found that the T_2 relaxation times (extracted from the linewidth) decreased with increasing the number of experiments performed on the same sample at the same detection field. (d) Temperature of the NMR sample after being placed near the two commercial magnetometers. In a typical ZULF NMR experiment, a sample spends an equal amount of time in a prepolarization magnet (at $\approx 22^\circ\text{C}$) and next to the two magnetometers which leads to the considerable heating of the liquid over long experiments.

ULF Relaxometry of Whole Blood and Plasma

In this part of the study, we used human whole blood and blood plasma to demonstrate the applicability of ULF NMR relaxometry for biological samples. Blood with all its components intact (white and red blood cells, platelets, and plasma, collected using a tube that contains an anticoagulant solution) is called whole blood. Blood plasma (45% of the whole blood) is the cell-free supernatant, which can be obtained by centrifuging whole blood. The high water content of whole blood and plasma allowed us to readily observe proton signals under ULF conditions.

Figure 5 shows that the amplitude of the proton signal was larger in plasma samples than in whole-blood samples. This is an effect of higher water content and slower proton relaxation in plasma compared to the whole blood, where the cellular component is dominated by hemoglobin-rich red blood cells⁵³. At 10 μT , proton relaxation times were determined as: $T_1^{\text{blood}} = 0.305(9)$ s, $T_2^{\text{blood}} = 0.295(2)$ s; $T_1^{\text{plasma}} = 0.39(3)$ s, $T_2^{\text{plasma}} = 0.304(1)$ s. As shown, the difference in T_1 between whole blood and plasma is higher than in T_2 , which reveals the stronger influence of the cell components on the T_1 relaxation and agrees with low-field NMR relaxometry³. Especially in venous whole-blood samples, intracellular heterogeneous distribution of the paramagnetic molecules, such as deoxygenated hemoglobin, might cause magnetic-susceptibility difference between the blood cell and plasma, which contributes to the T_2 relaxation by dephasing water-proton coherence⁵⁴. However, this mechanism becomes insignificant in ULF regime, which allows one to measure heterogeneous samples without susceptibility broadening⁵⁵.

To determine the limitations of the method, the ULF relaxation profile of human whole blood and blood plasma was measured. As shown in Fig. 5b,c, the T_1 and T_2 relaxation times of the protons in whole blood varied with the storage field (10-510 μT) without a specific pattern. This can be a result of a residual cellular metabolism which can change the protein content over time⁵⁶. In blood plasma, where no cellular metabolism is expected, the content of metabolites should remain stable over time.

In contrast to whole blood, in plasma, the decrease in the T_1 relaxation time of protons was observed with the variation of the storage field from 10 μ T to 510 μ T (Fig. 5b). This complicated dependence of the relaxation times on the storage field can be attributed to a sample heating in the proximity of an operating atomic magnetometer. Indeed, in our magnetic-field profile measurements, the storage field was increased step by step without changing the sample. Even though the T_2 relaxation time (extracted from the linewidth) was measured at the same detection field, we observed its decrease in the subsequent experiments (Fig. 5c). This additionally confirms the effect of temperature on the measured relaxation times. When the sample temperature was measured by thermocouple as a function of acquisition time (time the sample spent near the atomic magnetometers), we observed that it could exceed 40°C, as shown in Fig. 5d. Therefore, the repeated measurements might cause an increase in the temperature of the sample over time and could cause faster relaxation⁵⁷. To overcome this limitation, active cooling or/and temperature stabilization can be implemented in the setup to maintain temperature stability¹⁴. It should also be noted that the T_2 values are consistently lower than the T_1 values, which resulted from the additional contribution of low-frequency fluctuations such as slow molecular rotation, chemical exchange, and diffusion to the transverse relaxation².

Conclusions

In this work, ZULF NMR relaxometry was exploited to collect information about the molecular environment in chemical solutions and biofluids. The strong influence of paramagnetic oxygen on zero-field NMR spectroscopy was demonstrated by measuring spin systems with ^1H - ^{31}P and ^1H - ^{13}C couplings. In particular, we showed a strong dependence of the heteronuclear singlet-state lifetime on the concentration of dissolved oxygen. We also investigated the lifetime of ^{15}N -methylpyridinium, a precursor of potential contrast agents, in the ULF regime. In particular, we demonstrated slower longitudinal relaxation of this compound in H_2O compared to D_2O . Nuclear magnetic relaxation dispersion profiles of aqueous solutions of a paramagnetic compound (CuSO_4) were studied in the ULF regime. We demonstrated that samples with and without dissolved oxygen exhibit a slightly different magnetic-field dependence, which agrees well with the relaxation theory, proving the reliability and potential applicability of the method for chemical analysis. Finally, we investigated the ULF NMR spectra of human whole blood and blood plasma. Despite the shorter (≈ 300 ms) relaxation times of these biofluids, the high-quality ULF NMR spectra were obtained and examined. These measurements hold promise as a new blood diagnostic technique. Without the need for sophisticated sample preparation, the blood T_2 relaxation time obtained in short measurements (< 1 min) at the ULF conditions is a potentially valuable marker of inflammation often induced by metabolic disorders, infections, etc. Our work points towards the applicability of ZULF NMR relaxometry employing atomic magnetometers as a simple, portable, robust, inexpensive, and sensitive tool in chemical and biological analysis. In addition, ULF NMR relaxometry of biofluids paves the way for molecular imaging at ZULF conditions where T_1 and T_2 relaxation properties of specific molecules predominately determine image contrast⁵⁸⁻⁶¹.

Methods

Sample Preparation

Trimethyl phosphate (CAS# 512-56-1) and ^{13}C -formic acid (CAS# 1633-56-3) were purchased from Sigma-Aldrich. For each compound, four 0.2 ml neat liquid samples were prepared by transferring them into standard 5 mm NMR tubes. To investigate the effect of oxygen on relaxation times in each compound, one sample was sealed without being degassed. The other three samples were degassed once, twice, and three times using the freeze-pump-thaw method with the use of a two-stage vacuum pump. This allowed us to evacuate the gas above a sample to a gas-pressure of 10^{-6} mbar. After degassing, the tubes were flame-sealed under vacuum.

^{15}N -methylpyridinium was synthesized according to literature procedures starting from ^{15}N -enriched pyridine⁶² and dissolved in D_2O and H_2O by obtaining 5.5 M ^{15}N -methylpyridinium solutions. The solutions were transferred to 5 mm NMR tubes and then tubes were flame-sealed under vacuum following two freeze-pump-thaw cycles for degassing. For high-field relaxometry studies, ^{15}N -methylpyridinium was dissolved in D_2O and 1:4 D_2O and H_2O mixture at 5.5 M concentration. The samples were degassed prior to measurements.

Copper sulfate (CuSO_4) (CAS# 7758-98-7) was also purchased from Sigma-Aldrich. The CuSO_4 solutions with various concentrations were prepared by dissolving the compound in deionized water. For each concentration, 0.2 ml of solutions were placed inside two standard 5 mm NMR tubes. One of the tubes was sealed without degassing, and another tube was degassed twice using the freeze-pump-thaw method and then flame sealed. The pressure above the frozen liquid after the second cycle was below 10^{-4} mbar.

Human whole blood samples from healthy adults (male volunteers) were collected in tubes containing heparin as an an-

ticoagulant (volume ratio: 9:1) on the day of the experiment (blood came from the Regional Blood Transfusion Centre, Kraków, Poland). The volunteer donors had not taken any medicines for the two weeks prior to the withdrawal. Informed consent was given by each volunteer prior to the blood withdrawal and the study was in accordance with the principles outlined in the World Medical Association (WMA) Declaration of Helsinki, as well as Bioethical Commission of the Jagiellonian University. 300 μ L of whole blood were kept for the measurements. Remaining whole blood was subjected to centrifugation (acceleration of 800 g and run time: 15 min at room temperature, with soft stop) to separate plasma from the rest of the blood components. Plasma was collected and placed in Eppendorf tubes for further sample preparation procedures and measurements. 0.2 ml of whole blood and plasma were transferred to NMR tubes and flame-sealed without degassing. The samples were kept at 4°C to reduce the metabolism until measurement and measured up to an hour after blood withdrawal.

Experimental Setup

ZULF NMR experimental setup was built/designed by DM technologies. For the relaxation study using NMR at zero magnetic field, the NMR samples, prepolarized for about 20 s inside a permanent magnet (1.4 T), were mechanically shuttled to the zero-field region (interior of a multi-layer magnetic shield) through a guiding field (10 μ T) applied by the solenoid (Fig. S1). After transfer to the detection region, the samples were stored in the guiding field of the solenoid (storage field) for variable times (from 1 s to 15 s). After that time, the storage field was switched off and an optimal transverse pulse was applied to generate a zero-field NMR signal of maximum amplitude³⁴. For the ^1H - ^{13}C spin system, the optimal pulse-induced rotation angle was 4π for the ^1H spins, while in the ^1H - ^{31}P system, the maximum amplitude was achieved using 5π pulse angle for the ^1H spins. To investigate the relaxation of water protons in CuSO_4 solutions, whole blood, plasma, and ^{15}N -coupled-proton relaxation in ^{15}N -methylpyridinium solutions, ULF NMR spectroscopy was used (Fig. S1). In these cases, after 15 s thermal prepolarization with the 1.4 T permanent magnet, the samples were transferred to the detection region (inside the magnetic shield), where it was stored in various guiding fields (10–510 μ T) and times (0.5–6.05 s). Then the guiding field was switched off (within 10 μ s) while a detection field of 0.8 μ T, corresponding to about 34 Hz of precession of ^1H , was applied in a transverse direction to the sensitive axis of the magnetometer for water-proton relaxation studies. In the ^{15}N -coupled-proton relaxation measurements, the detection field was adjusted to 1.88 μ T (corresponding to 80 Hz of ^1H precession). The detection fields were chosen in such a way that the proton-precession signal appeared in a convenient spectral region, i.e., far from 50 Hz magnetic noise and its overtones but also away from low-frequency flicker noise. It should be noted that a further increase in the solenoid storage field could introduce field inhomogeneities, which may affect the T_2 relaxation. Detailed schematics of our ULF NMR experimental setup and the experimental sequence are shown in Supplementary Information. In the T_1 studies, each data point was obtained after averaging 4–16 transients and is presented with a standard deviation as an error bar. The transverse longitudinal relaxation times T_2 were calculated from the linewidths of the peaks in the spectra. Full maximum half-width (FWHM) values were derived by fitting NMR spectra to the Lorentzian function. Standard-deviation errors of the fitting parameter are denoted with error bars. Data processing and data analysis were performed using custom Python scripts described in Ref.³⁴.

High-field T_1 measurement on ^{15}N -methylpyridinium samples was performed via an inversion recovery experiment on a 7 T Bruker NMR system with Avance III console.

Acknowledgements

The authors acknowledge the support from the European Union's Horizon 2020 research and innovation program under the Marie Skłodowska-Curie grant agreement No. 766402. The authors thank Anil P. Jagtap and Gabriele Stevanato for the synthesis of ^{15}N -methylpyridinium and the high-field T_1 measurements of ^{15}N -methylpyridinium. D.B. thanks James McMillen for stimulating discussions and the Alexander von Humboldt Foundation (Sofja Kovalevskaja Award) for financial support. This research was partially supported by the Excellence Initiative - Research University Program at the Jagiellonian University in Kraków.

Author contributions statement

S.A., P.P., D.B., and S.P. purposed the study. S.A., A.K., F.C.A., and J.D. prepared the samples. P.P. constructed experimental apparatus. S.A., A.K., and P.P. conducted the experiments and analysed the results. S.P., D.B., and S.G. contributed to discussion of the experimental results. S.P. supervised the overall research effort. S.A., P.P., and A.K. wrote the manuscript. All authors reviewed the manuscript.

Additional information

There are no conflicts to declare.

References

1. Kimmich, R. *NMR Tomography, Diffusometry, Relaxometry* (Springer Berlin, Heidelberg, 2019).
2. Levitt, M. H. *Spin dynamics: basics of nuclear magnetic resonance* (John Wiley & Sons, 2013).
3. Cistola, D. P. & Robinson, M. D. Compact NMR relaxometry of human blood and blood components. *TrAC Trends Anal. Chem.* **83**, 53–64 (2016).
4. Colnago, L. A. *et al.* Low field, time domain NMR in the agriculture and agrifood sectors: An overview of applications in plants, foods and biofuels. *J. Magn. Reson.* **323**, 106899 (2021).
5. Barbosa, L. L. *et al.* Application of low-field NMR for the determination of physical properties of petroleum fractions. *Energy & Fuels* **27**, 673–679 (2013).
6. Hills, B. Applications of low-field NMR to food science. *Annu. Reports on NMR Spectrosc.* **58**, 177–230 (2006).
7. Johnson, C. *et al.* Magnetic relaxometry with an atomic magnetometer and SQUID sensors on targeted cancer cells. *J. Magn. Mater.* **324**, 2613–2619 (2012).
8. Ganssle, P. J. *et al.* Ultra-low-field NMR relaxation and diffusion measurements using an optical magnetometer. *Angewandte Chemie Int. Ed.* **53**, 9766–9770 (2014).
9. Tayler, M. C., Ward-Williams, J. & Gladden, L. F. NMR relaxation in porous materials at zero and ultralow magnetic fields. *J. Magn. Reson.* **297**, 1–8 (2018).
10. Volegov, P. *et al.* *Magnetic Resonance Relaxometry at Low and Ultra Low Fields* (IFMBE Proc., 2010).
11. Tayler, M. C. D. *et al.* Invited Review Article: Instrumentation for nuclear magnetic resonance in zero and ultralow magnetic field. *Rev. Sci. Instruments* **88**, 091101 (2017).
12. Greenberg, Y. S. Application of superconducting quantum interference devices to nuclear magnetic resonance. *Rev. Mod. Phys.* **70**, 175–222 (1998).
13. Put, P. *et al.* Zero- to ultralow-field NMR spectroscopy of small biomolecules. *Anal. Chem.* **93**, 3226–3232 (2021).
14. Bodenstedt, S., Mitchell, M. & Tayler, M. Fast-field-cycling ultralow-field nuclear magnetic relaxation dispersion. *Nat. Commun.* **12**, 4041 (2021).
15. Kimmich, R. Field cycling in NMR relaxation spectroscopy: Applications in biological, chemical and polymer physics. *Bull. Magn. Reson.* **1**, 195–218 (1980).
16. Kimmich, R. *Field-cycling NMR relaxometry: instrumentation, model theories and applications* (Royal Society of Chemistry, 2018).
17. Lane, T. J., Shukla, D., Beauchamp, K. A. & Pande, V. S. To milliseconds and beyond: challenges in the simulation of protein folding. *Curr. Opin. Struct. Biol.* **23**, 58–65 (2013).
18. Chung, H. S., Khalil, M., Smith, A. W., Ganim, Z. & Tokmakoff, A. Conformational changes during the nanosecond-to-millisecond unfolding of ubiquitin. *Proc. Natl. Acad. Sci.* **102**, 612–617 (2005).
19. Cong, Y. *et al.* Mass spectrometry-based monitoring of millisecond protein–ligand binding dynamics using an automated microfluidic platform. *Lab Chip* **16**, 1544–1548 (2016).
20. Lindahl, E. & Sansom, M. S. Membrane proteins: molecular dynamics simulations. *Curr. Opin. Struct. Biol.* **18**, 425–431 (2008). Membranes / Engineering and design.
21. Waldauer, S. A., Bakajin, O. & Lapidus, L. J. Extremely slow intramolecular diffusion in unfolded protein I. *Proc. Natl. Acad. Sci.* **107**, 13713–13717 (2010).
22. Olivo, G. *et al.* Following a chemical reaction on the millisecond time scale by simultaneous x-ray and uv/vis spectroscopy. *The J. Phys. Chem. Lett.* **8**, 2958–2963 (2017).
23. Bhattacharjee, A. *et al.* Picosecond to millisecond tracking of a photocatalytic decarboxylation reaction provides direct mechanistic insights. *Nat. Commun.* **10**, 5152 (2019).
24. Rangadurai, A., Szymaski, E. S., Kimsey, I. J., Shi, H. & Al-Hashimi, H. M. Characterizing micro-to-millisecond chemical exchange in nucleic acids using off-resonance r1p relaxation dispersion. *Prog. Nucl. Magn. Reson. Spectrosc.* **112–113**, 55–102 (2019).
25. Parigi, G., Ravera, E., Fragai, M. & Luchinat, C. Unveiling protein dynamics in solution with field-cycling NMR relaxometry. *Prog. Nucl. Magn. Reson. Spectrosc.* **124–125**, 85–98 (2021).

26. Skewis, L. R. *et al.* T₂ Magnetic Resonance: A Diagnostic Platform for Studying Integrated Hemostasis in Whole Blood—Proof of Concept. *Clin. Chem.* **60**, 1174–1182 (2014).
27. Neely, L. A. *et al.* T₂ magnetic resonance enables nanoparticle-mediated rapid detection of candidemia in whole blood. *Sci. Transl. Medicine* **5**, 182ra54 (2013).
28. Wang, Z. *et al.* Detection of metabolite–protein interactions in complex biological samples by high-resolution relaxometry: Toward interactomics by NMR. *J. Am. Chem. Soc.* **143**, 9393–9404 (2021).
29. Schuhmacher, J. H. *et al.* NMR relaxation times T₁ and T₂ of water in plasma from patients with lung carcinoma: Correlation of T₂ with blood sedimentation rate. *Magn. Reson. Medicine* **5**, 537–547 (1987).
30. Masiewicz, E. *et al.* Towards applying NMR relaxometry as a diagnostic tool for bone and soft tissue sarcomas: a pilot study. *Sci. Reports* **10** (2020).
31. Ledbetter, M. *et al.* Optical detection of nmr j-spectra at zero magnetic field. *J. Magn. Reson.* **199**, 25–29 (2009).
32. Kjaer, L. *et al.* Evaluation of relaxation time measurements by magnetic resonance imaging. *Acta Radiol.* **28**, 345–351 (1987).
33. Benedek, G. B. & Purcell, E. M. Nuclear magnetic resonance in liquids under high pressure. *The J. Chem. Phys.* **22**, 2003–2012 (1954).
34. Alcicek, S., Put, P., Kontul, V. & Pustelny, S. Zero-field NMR J-spectroscopy of organophosphorus compounds. *The J. Phys. Chem. Lett.* **12**, 787–792 (2021).
35. Levitt, M. H. Singlet nuclear magnetic resonance. *Annu. Rev. Phys. Chem.* **63**, 89–105 (2012).
36. Emondts, M. *et al.* Long-lived heteronuclear spin-singlet states in liquids at a zero magnetic field. *Phys. Rev. Lett.* **112**, 077601 (2014).
37. Theis, T. *et al.* Chemical analysis using J-coupling multiplets in zero-field NMR. *Chem. Phys. Lett.* **580**, 160 – 165 (2013).
38. Blanchard, J. W. & Budker, D. Zero- to ultralow-field NMR. *eMagRes* **5**, 1395 – 1410 (2016).
39. Barskiy, D. *et al.* Zero-field nuclear magnetic resonance of chemically exchanging systems. *Nat. Commun.* **10**, 3002 (2019).
40. Alcicek, S., Put, P., Barskiy, D., Kontul, V. & Pustelny, S. Zero-field NMR of urea: Spin-topology engineering by chemical exchange. *The J. Phys. Chem. Lett.* **12**, 10671–10676 (2021).
41. Livo, K., Prasad, M. & Graham, T. Quantification of dissolved O₂ in bulk aqueous solutions and porous media using NMR relaxometry. *Sci. Reports* **11**, 1–9 (2021).
42. Nestle, N., Baumann, T. & Niessner, R. Oxygen determination in oxygen-supersaturated drinking waters by NMR relaxometry. *Water Res.* **37**, 3361–3366 (2003).
43. Tayler, M. C. & Gladden, L. F. Scalar relaxation of NMR transitions at ultralow magnetic field. *J. Magn. Reson.* **298**, 101–106 (2019).
44. Tayler, M. C. D., Ward-Williams, J. & Gladden, L. F. Ultralow-field nuclear magnetic resonance of liquids confined in ferromagnetic and paramagnetic materials. *Appl. Phys. Lett.* **115**, 072409 (2019).
45. Jagtap, A. P., Kaltschnee, L. & Glöggler, S. Hyperpolarization of ¹⁵N-pyridinium and ¹⁵N-aniline derivatives by using parahydrogen: new opportunities to store nuclear spin polarization in aqueous media. *Chem. Sci.* **10**, 8577–8582 (2019).
46. Bagno, A., Gerard, S., Kevelam, J., Menna, E. & Scorrano, G. Detecting hydrogen bonding by NMR relaxation of the acceptor nuclei. *Chem. - A Eur. J.* **6**, 2915–2924 (2000).
47. Kakihana, M., Okamoto, M. & Nagumo, T. Isotope effects on deuterium spin-lattice relaxation in H₂O/D₂O mixtures. *Zeitschrift für Naturforschung A* **40**, 1085–1095 (1985).
48. Holz, M. D₂O-H₂O isotope effect on nuclear magnetic relaxation of alkali halide nuclei and preferential solvation in mixed solvents. *J. Chem. Soc., Faraday Trans. 1* **74**, 644–656 (1978).
49. Blanchard, J., Teng, W., Eills, J., Hu, Y. & Budker, D. Zero- to ultralow-field nuclear magnetic resonance J-spectroscopy with commercial atomic magnetometers. *J. Magn. Reson.* **314**, 106723 (2020).
50. Put, P. *et al.* Detection of pyridine derivatives by SABRE hyperpolarization at zero field. *ChemXiv. Prepr.* (2022).
51. Bloembergen, N., Purcell, E. M. & Pound, R. V. Relaxation effects in nuclear magnetic resonance absorption. *Phys. Rev.* **73**, 679–712 (1948).

52. Köylü, M. Z., Asubay, S. & Yilmaz, A. Determination of proton relaxivities of Mn(II), Cu(II) and Cr(III) added to solutions of serum proteins. *Molecules* **14**, 1537–1545 (2009).
53. Kang, Y. S., Gore, J. C. & Armitage, I. M. Studies of factors affecting the design of NMR contrast agents: manganese in blood as a model system. *Magn. Reson. Medicine* **1**, 396–409 (1984).
54. Gomori, J., Grossman, R. & Asakura, T. NMR2 relaxation times of blood: dependence on field strength, oxidation state, and cell integrity. *J. computer assisted tomography* **11**, 684–690 (1987).
55. Burueva, D. *et al.* Chemical reaction monitoring using zero-field nuclear magnetic resonance enables study of heterogeneous samples in metal containers. *Angewandte Chemie Int. Ed.* **59**, 17026 – 17032 (2020).
56. Ghini, V., Quaglio, D., Luchinat, C. & Turano, P. NMR for sample quality assessment in metabolomics. *New Biotechnol.* **52**, 25–34 (2019).
57. Vesanen, P. T. *et al.* Temperature dependence of relaxation times and temperature mapping in ultra-low-field MRI. *J. Magn. Reson.* **235**, 50–57 (2013).
58. Hori, S. *et al.* Magnetic shieldless ultra-low-field MRI with an optically pumped magnetometer. *J. Magn. Reson.* **343**, 107280 (2022).
59. Savukov, I. *et al.* MRI with an atomic magnetometer suitable for practical imaging applications. *J. Magn. Reson.* **199**, 188–191 (2009).
60. Waddington, D. E. J., Boele, T., Maschmeyer, R., Kuncic, Z. & Rosen, M. S. High-sensitivity in vivo contrast for ultra-low field magnetic resonance imaging using superparamagnetic iron oxide nanoparticles. *Sci. Adv.* **6**, eabb0998 (2020).
61. Bevilacqua, G., Biancalana, V., Dancheva, Y. & Vigilante, A. Sub-millimetric ultra-low-field MRI detected in situ by a dressed atomic magnetometer. *Appl. Phys. Lett.* **115**, 174102 (2019).
62. Zafar, A. *et al.* Synthesis, structural analysis, electrochemical and magnetic properties of tetrachloroferrate ionic liquids. *New J. Chem.* **45**, 13429–13440 (2021).